Supporting Information

Anion-modulated CoP electrode as bifunctional electrocatalyst for anion-exchange membrane hydrazine-assisted water electrolyser

Kaixun Li[a], Yun Tong[a], JinFeng He[a], Xiang-Yang Liu[b]*, and Pengzuo Chen[a]**

[a] School of Chemistry and Chemical Engineering, Key Laboratory of Surface & Interface Science of Polymer Materials of Zhejiang Province, Zhejiang Sci-Tech University, Hangzhou 310018, China

[b] College of Chemistry and Material Science, Sichuan Normal University, Chengdu 610068, China

Correspondence and requests for materials should be addressed to Y. Tong, X. Y. Liu and P. Z. Chen (E-mail: tongyun@mail.ustc.edu.cn; xiangyangliu@sicnu.edu.cn; pzchen0421@126.com)

Table of contents

Figure S1 (a-d) The SEM images of F-CoP/CF sample. 7

Figure S2 (a-d) The SEM images of Cl-CoP/CF sample. 8

Figure S3 (a-b) The SEM images of Br-CoP/CF sample. 9

Figure S4 The cyclic voltammetry curves of (a) F-CoP/CF, (b) Cl-CoP/CF, (c) Br-CoP/CF and (d) CF electrodes in 1.0 M KOH recorded at different scan rates from 20 to 100 mV s^{-1}. 10

Figure S5 (a) The XPS survey and the high-resolution (b) F 1s spectra of F-CoP/CF sample. 11

Figure S6 (a) The XPS survey and the high-resolution (b) Cl 2p spectra of Cl-CoP/CF sample. .. 11

Figure S7 (a) The XPS survey and the high-resolution (b) Br 3d spectra of Br-CoP/CF sample. . 12

Figure S8 The XPS spectra of (a) Co 2p and (b) P 2p for the F-CoP/CF, Cl-CoP/CF and Br-CoP/CF samples. 12

Figure S9 (a-b) The SEM images of unmodified CoP/CF sample. 13

Figure S10 Nyquist plots of $Co(OH)_2$/CF, CoP/CF and F-CoP/CF. 13

Figure S11 The HER performance for F-CoP samples on different substrates. 14

Figure S12 The HER performance of F-CoP/CF with different loading mass. 14

Figure S13 Comparison of HER performance of F-CoP/CF synthesized from different usages of NH_4F. 15

Figure S14 LSV curves of F-CoP/CF before and after 3000 cycles for HzOR. 15

Figure S15 (a) The XRD pattern and (b-d) XPS spectra of F-CoP/CF sample after the stability test of HER. 16

Figure S16 (a-d) The SEM images of F-CoP/CF sample after the stability test of HER. 17

Figure S17 (a) The XRD pattern and (b-d) XPS spectra of F-CoP/CF sample after the stability test of HzOR. 18

Figure S18 (a-d) The SEM images of F-CoP/CF sample after the stability test of HzOR. 19

Table S1 The fitting data of EIS spectra for the prepared catalysts for HER. 20

Table S2 The fitting data of EIS spectra for the prepared catalysts for HzOR. 20

Table S3 Comparisons of HER performance of our catalysts with various kinds of reported earth abundant electrocatalysts. 21

Table S4 Performance comparisons of water splitting of our catalysts with other reported bifunctional electrodes. 22

References 23

Experimental Section

Materials: From Country Shuanglin Chemical, we obtain hydrochloric acid (HCl, AR). Aladdin is the source for the following chemicals: potassium hydroxide (KOH, AR), sodium hypophosphite monohydrate ($NaH_2PO_2·H_2O$, AR), absolute ethanol (C_2H_5OH, 99.7%), cobalt nitrate (II) hexahydrate ($Co(NO_3)_2·6H_2O$, 98%), ammonium chloride (NH_4Cl, AR), ammonium bromide (NH_4Br, AR) and ammonium fluoride (NH_4F, AR). McLean, Inc. provides sodium acetate (CH_3COONa, AR) for sale. SaiBo electrochemical material network sells Ni foams with a 1.0 mm thickness. None of the compounds are processed further before usage.

Synthesis of F-CoP/CF, Br-CoP/CF and Br-CoP/CF electrodes: F-CoP electrocatalyst is prepared by electrostatic potential electrodeposition. The electrocatalysts are supported on a substrate of 1 cm×2 cm copper foam (CF). Prior to synthesis, CF is rinsed three times successively with deionized water and ethanol after 15 minutes of immersion in 20 % hydrochloric acid. The electrodeposition bath used to create the F-CoP electrocatalyst contained 3 g NH_4F, 1.5 g of $Co(NO_3)_2$, 6 g of $NaH_2PO_2·H_2O$, and 1 g of sodium acetate in 50 mL of deionized water. A three-electrode device with Ag/AgCl and graphite rod as reference and counter electrodes, is the initial stage in the electrodeposition process. By using a CF working electrode and applying a constant voltage of -2 V for 30 min, an F-CoP/CF electrode is created. Then alternate rinse with deionized water and ethanol three times. The synthesis of Cl-CoP/CF and Br-CoP/CF is similar to that of F-CoP/CF, which can be obtained by replacing NH_4F with NH_4Cl and NH_4Br, respectively. The electrodes with different loading mass are prepared by changing electrodeposition time (5, 10, 15, 20, 25 and 35 min). In addition, series of F-CoP/CF electrodes are prepared by using different amount of ammonium, and the synthesis procedure is the same as above.

Synthesis of $Co(OH)_2$/CF electrode: $Co(OH)_2$ is electrodeposited on CF by a constant voltage test. Typically, the electrodeposition bath is consist of 1.5 g $Co(NO_3)_2·6H_2O$. The Ag/AgCl and graphite

rod are used as reference and counter electrodes, and the treated CF is used as working electrodes. The final $Co(OH)_2$/CF is obtained by operating electrodeposition voltage of -2 V for 30 min. After that, the samples are rinsed three times by using a combination of ethanol and deionized water.

Synthesis of CoP/CF electrode: CoP/CF electrode is synthesized by annealing treatment. The synthesized $Co(OH)_2$/CF electrode and 400 mg $NaH_2PO_2 \cdot H_2O$ are placed in two porcelain vessels on the upper and lower sides of the tubular furnace. $Co(OH)_2$/CF is phosphating by annealing at 350 ℃ for 2 h in N_2 atmosphere. The heating rate is 5 ℃ min^{-1}. Next, perform a three-time alternating rinse using ethanol and deionized water, the CoP/CF electrode can be obtained after drying.

Material Characterizations: To examine the phase compositions and crystal structure of catalysts, powder X-ray diffraction (PXRD) is carried out on a DX-2700 diffractometer (Dandong Haoyuan Instrument Co. Ltd., China). The step size is 2943 and measurement time is 617.4 s with a pace of 0.2 s/step. Using a scanning electron microscope (SEM, Hitachi SU8I00) and high-resolution transmission electron microscopy, the surface morphology and content are examined (HRTEM). To confirm the chemical states of the elements in the samples, X-ray photoelectron spectroscopy (XPS) is performed on a PHI5300 apparatus using monochromatic Mg K as the source of radiation.

Electrochemical measurements: A three-electrode arrangement is used to conduct electrochemical experiments. Working electrodes are made of self-supported materials, whereas reference and counter electrodes are made of saturated calomel and graphite rod, respectively. The HzOR performance is measured in 1.0 M KOH with 0.2 M N_2H_4 electrolyte, while the HER and OER performance are studied in a 1.0 M KOH electrolyte by linear sweep voltammetry (LSV, scan rate of 5 mV s^{-1}). The potential of the reversible hydrogen electrode is obtained from all the results using the following equation: $E_{(vs.\ RHE)} = E_{(vs.\ Hg/HgCl2)} + E_{(Hg/HgCl2)}$ (0.241V) + 0.059 pH. The electrochemical impedance spectroscopy (EIS) are collected under an AC voltage model at a fixed overpotential in a frequency range of (10^{-2}-10^5 Hz). By using CV curves with scanning rates of 20, 40, 60, 80, and 100 mV s^{-1}, the electrochemical double-layer capacitance (C_{dl}) is calculated. All of the data are given after IR-correction.

Calculation method: To gain further insight into the intrinsic mechanism for the catalytic performance enhancement due to defects, density functional theory (DFT) calculations of a model of

CoP with without substitution of P by F were carried out. DFT based first-principles calculations are performed using the projected augmented wave (PAW)[1] method implemented in the Vienna ab initio simulation package (VASP)[2,3]. The Kohn-Sham one-electron states are expanded using the plane wave basis set with a kinetic energy cutoff of 400 eV. The Perdew-Burke-Ernzerhof (PBE)[4,5] exchange-correlation functional within the generalized gradient approximation (GGA) is employed. As the active surface, The CoP (001) surface is modeled by a periodic slab repeated in * surface unit cell. A P atom on the second layer is replaced by an F atom to simulate the doping of F atoms in the CoP. The Brillouin-zone (BZ) integration is carried out using the Monkhorst-Pack[6] sampling method with a density of 4×4×1 for the geometry optimizations. A vacuum layer of greater than 15 Å is included to avoid the interaction between neighboring slabs. All atoms are fully relaxed until the maximum magnitude of the force acting on the atoms is smaller than -0.05 eV/Å

The oxidation of hydrazine into nitrogen and hydrogen occurs in the following six consecutive elementary steps:

(A)* + N_2H_4 → *N_2H_4 (1)

(B)*N_2H_4 → *N_2H_3 + H^+ + e^- (2)

(C)*N_2H_3 →*N_2H_2 + H^+ + e^- (3)

(D)*N_2H_2 → *N_2H + H^+ + e^- (4)

(E)*N_2H → *N_2 + H^+ + e^- (5)

(F)*N_2 → * + N_2 (6)

The asterisk(*) represents the reaction surface of these calculated CoP (001), F-doped CoP (001). *N_2H_4, *N_2H_3, *N_2H_2, *N_2H and *N_2 denote the models with the corresponding chemisorbed species residing in the reaction surfaces. Among these six elementary steps, steps (A) and (F) are the adsorption of N_2H_4 and desorption of N_2, respectively. The other four elementary steps involve the generation of one proton and one electron. Then, using the computational hydrogen electrode (p = 1 atm, T = 298 K)[7], the Gibbs free energy of H^+ + e^- was replaced implicitly with the Gibbs free energy of one-half a H_2 molecule. Thus the reaction Gibbs free energies can be calculated with equations[8]:

$\Delta G_A = \Delta G_{*N2H4} - \Delta G_* - \Delta G_{N2H4}$ (7)

$\Delta G_B = \Delta G_{*N2H3} + 0.5\Delta G_{*H2} - \Delta G_{*N2H4}$ (8)

$\Delta G_C = \Delta G_{*N2H2} + 0.5\Delta G_{*H2} - \Delta G_{*N2H3}$ (9)

$\Delta G_D = \Delta G_{*N2H} + 0.5\Delta G_{*H2} - \Delta G_{*N2H2}$ (10)

$\Delta G_E = \Delta G_{*N2} + 0.5\Delta G_{*H2} - \Delta G_{*N2H}$ (11)

$\Delta G_F = \Delta G_{*} + \Delta G_{N2} - \Delta G_{*N2}$ (12)

The adsorption or reaction Gibbs free energy is defined as: $\Delta G = \Delta E + (ZPE - T\Delta S)$, where ΔE is the adsorption or reaction energy based on DFT calculations, ΔZPE is the zero point energy (ZPE) correction, T is the temperature, and ΔS is the entropy change. The entropies of gas phase H_2, N_2, and NH_2NH_2 are obtained from the NIST database[9] with standard condition, and the adsorbed species were only taken vibrational entropy (Sv) into account, as shown in the following formula:

$$Sv = \sum_i R\{hv_i/[k_B T^* \exp(hv_i/k_B T) - k_B T] - In[1 - \exp(-hv_i/k_B T)]\} \quad (13)$$

Among which R=8.314 J mol^{-1} K^{-1}, T=298.15 K, h=6.63×10^{-34} J s, k_B=1.38×10^{-23} J K^{-1}, i is the frequency number, v_i is the vibrational frequency (unit is cm^{-1}).

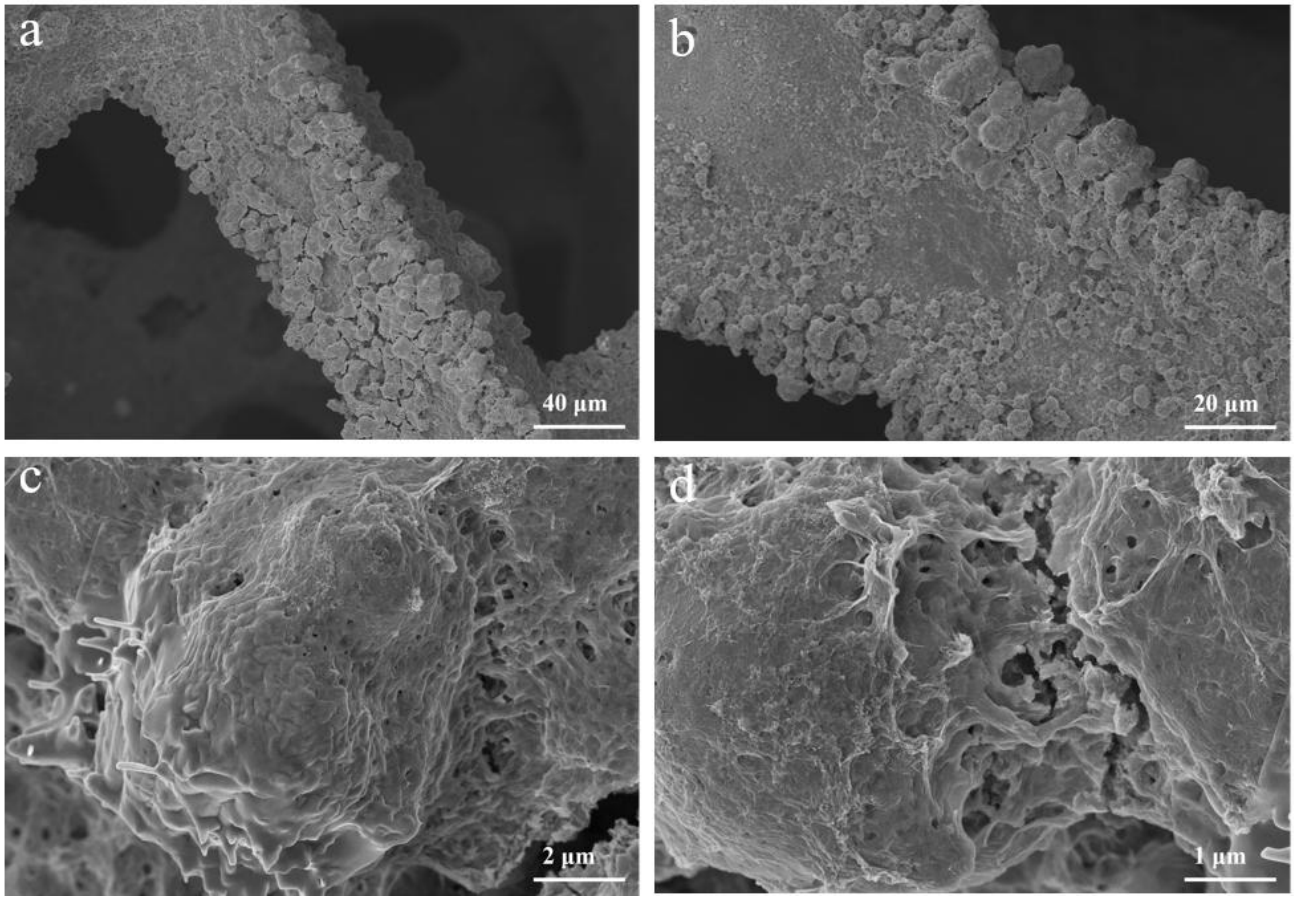

Figure S1 (a-d) The SEM images of F-CoP/CF sample.

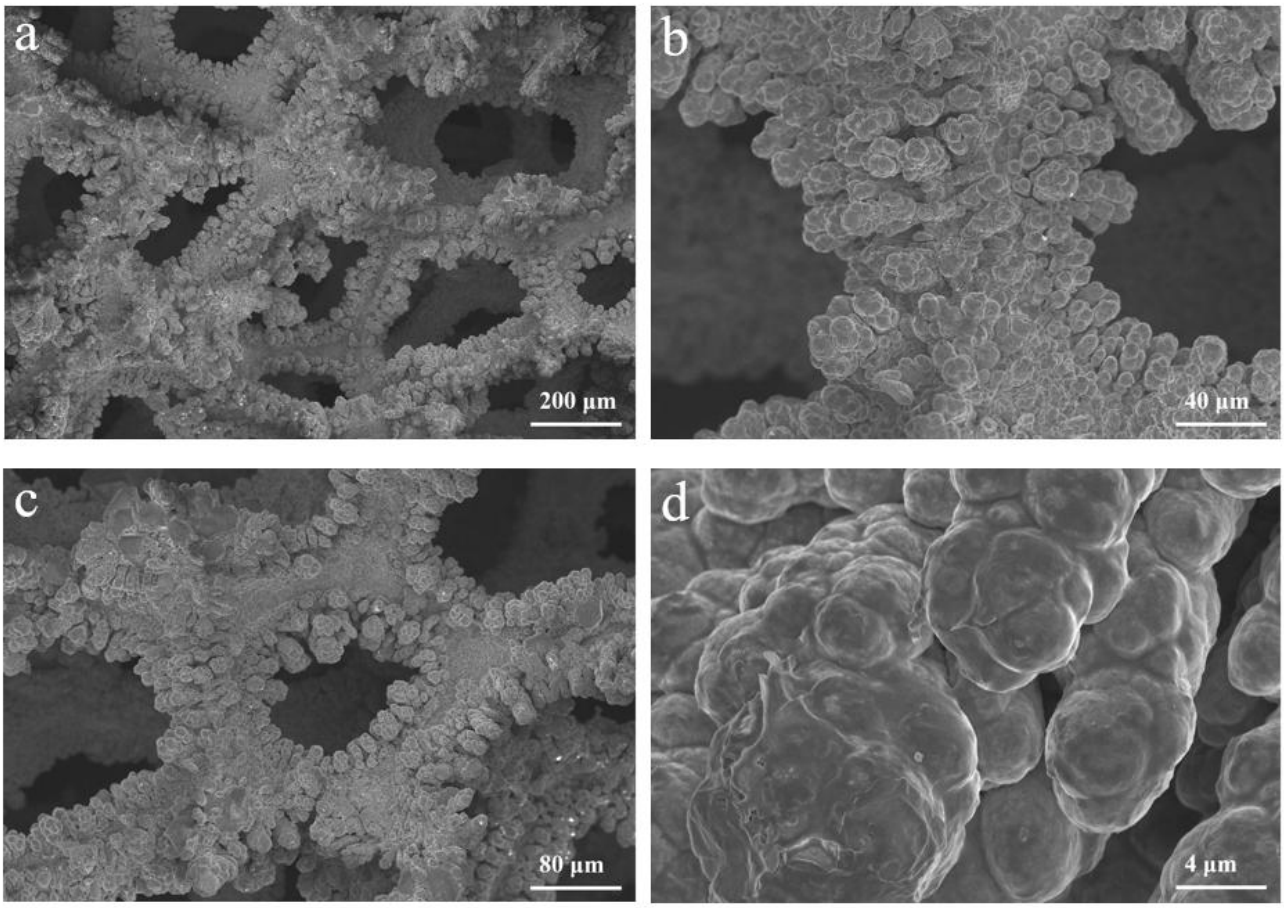

Figure S2 (a-d) The SEM images of Cl-CoP/CF sample.

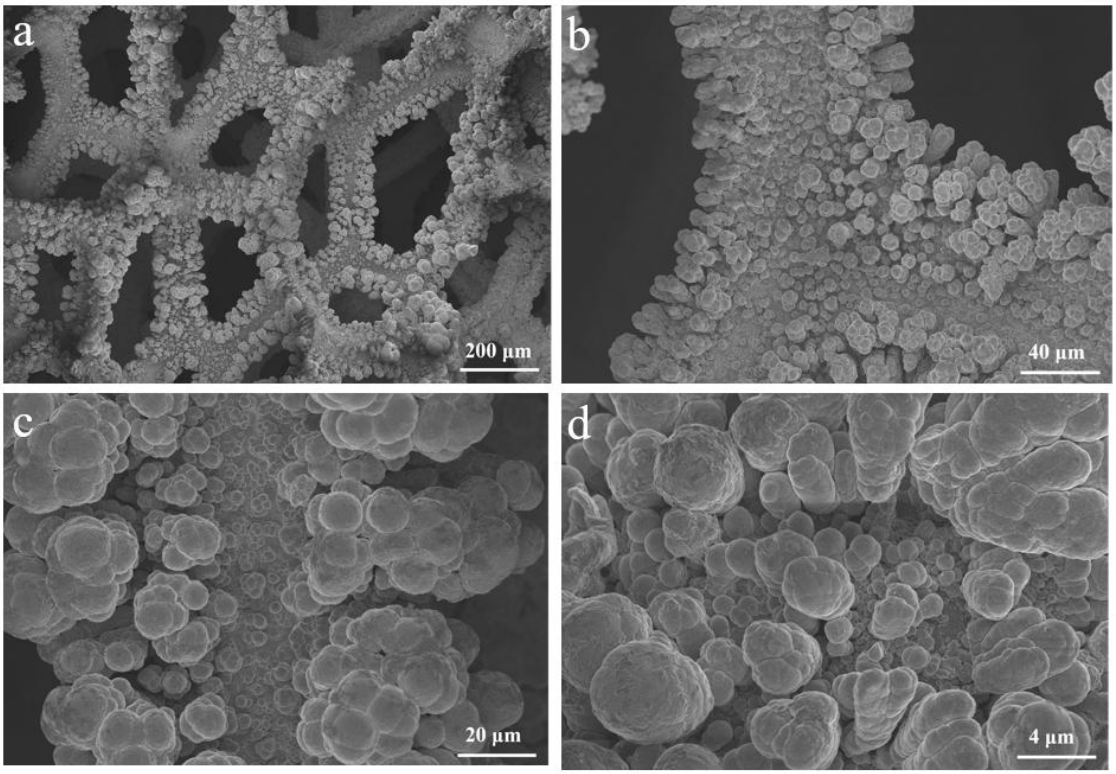

Figure S3 (a-b) The SEM images of Br-CoP/CF sample.

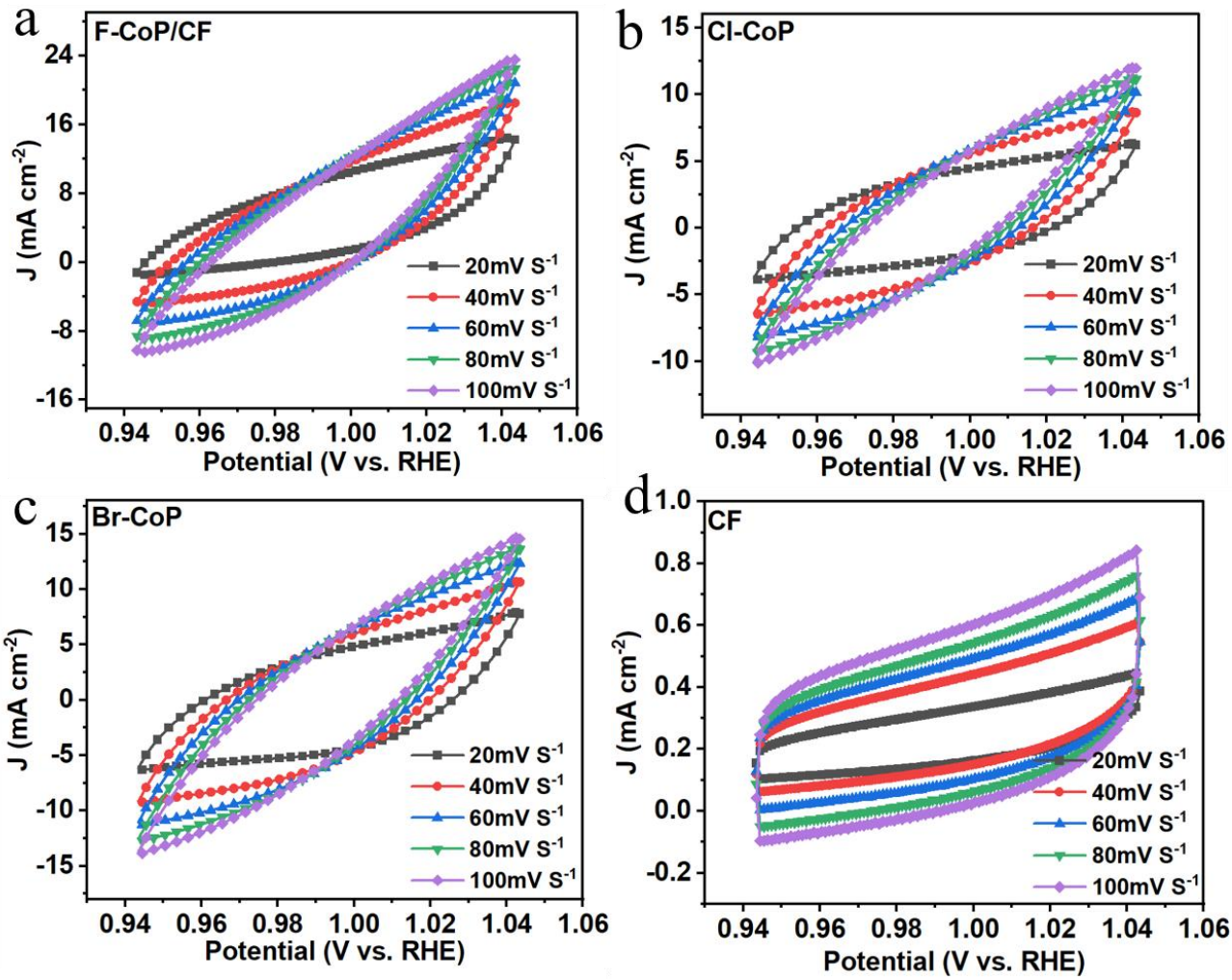

Figure S4 The cyclic voltammetry curves of (a) F-CoP/CF, (b) Cl-CoP/CF, (c) Br-CoP/CF and (d) CF electrodes in 1.0 M KOH recorded at different scan rates from 20 to 100 mV s^{-1}.

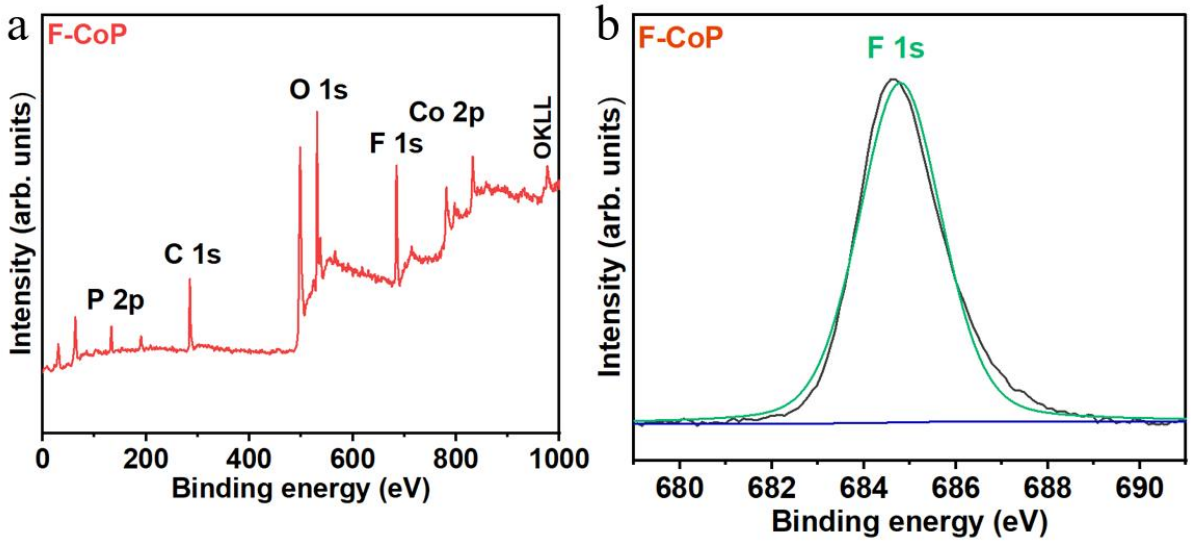

Figure S5 (a) The XPS survey and the high-resolution (b) F 1s spectra of F-CoP/CF sample.

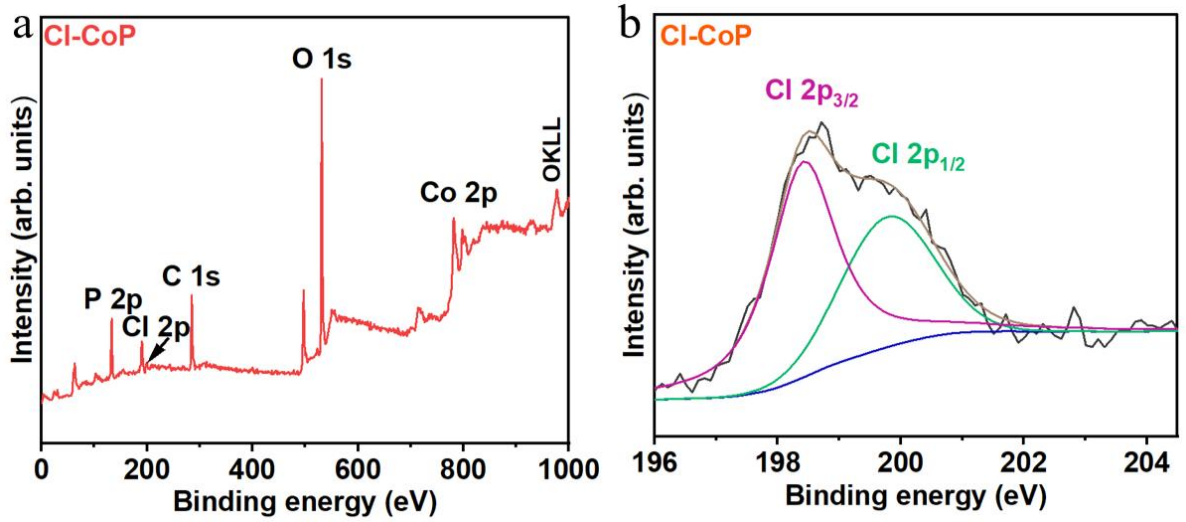

Figure S6 (a) The XPS survey and the high-resolution (b) Cl 2p spectra of Cl-CoP/CF sample.

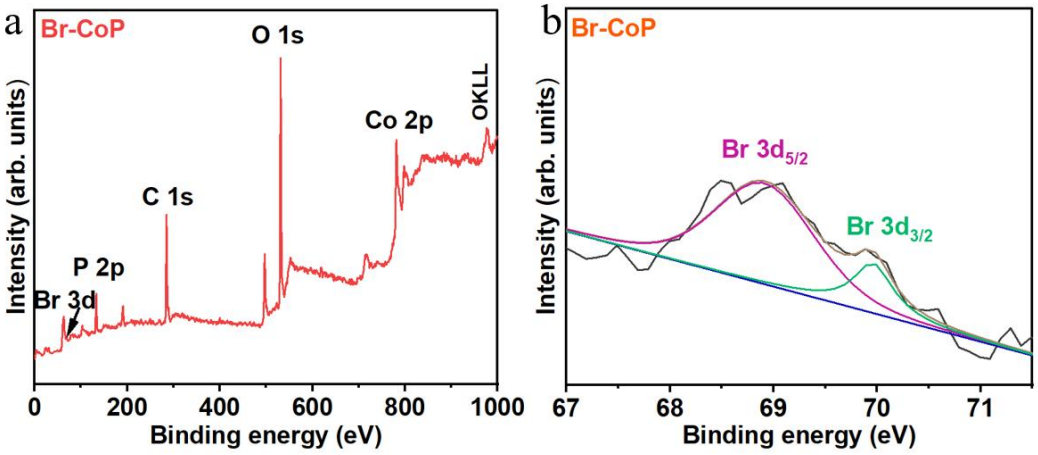

Figure S7 (a) The XPS survey and the high-resolution (b) Br 3d spectra of Br-CoP/CF sample.

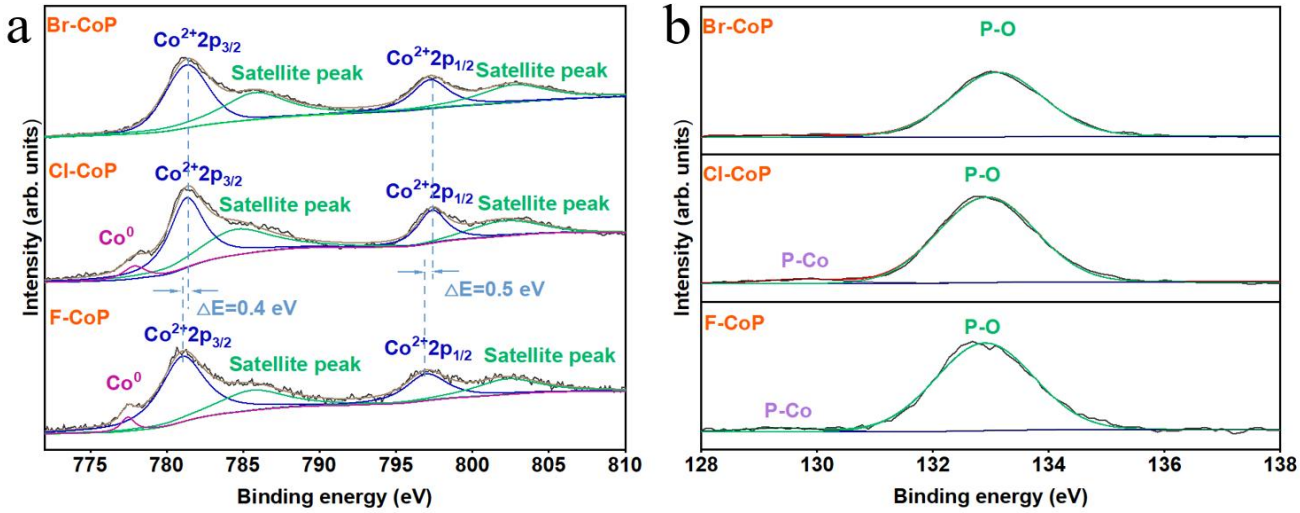

Figure S8 The XPS spectra of (a) Co 2p and (b) P 2p for the F-CoP/CF, Cl-CoP/CF and Br-CoP/CF samples.

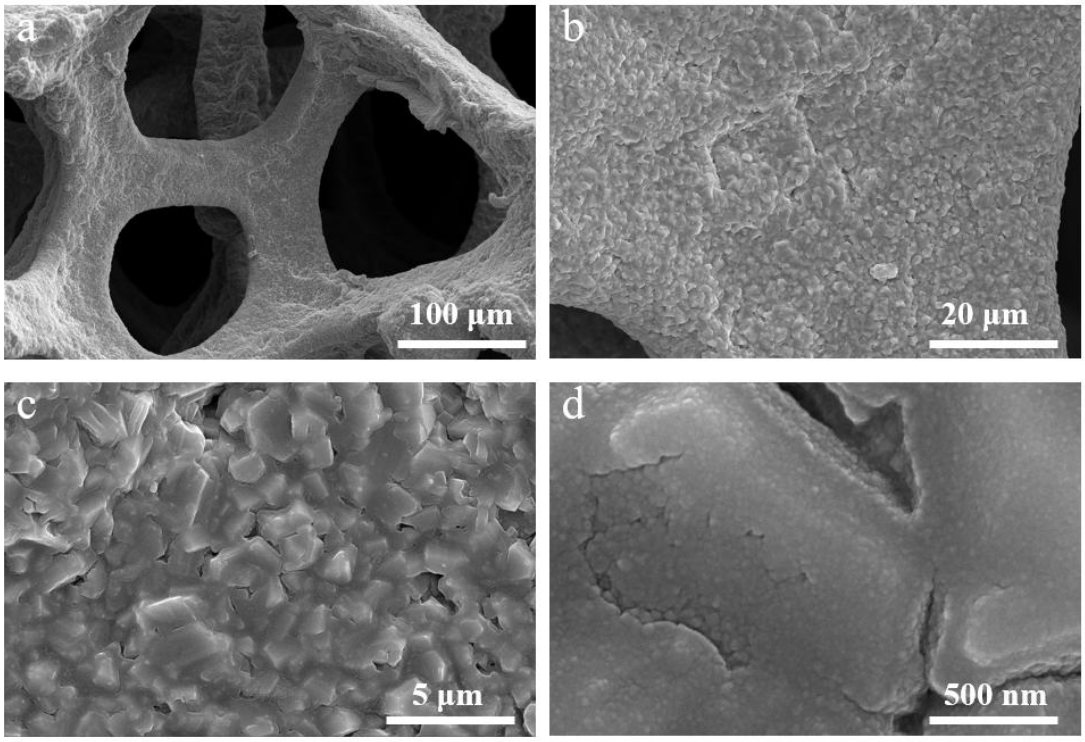

Figure S9 (a-b) The SEM images of unmodified CoP/CF sample.

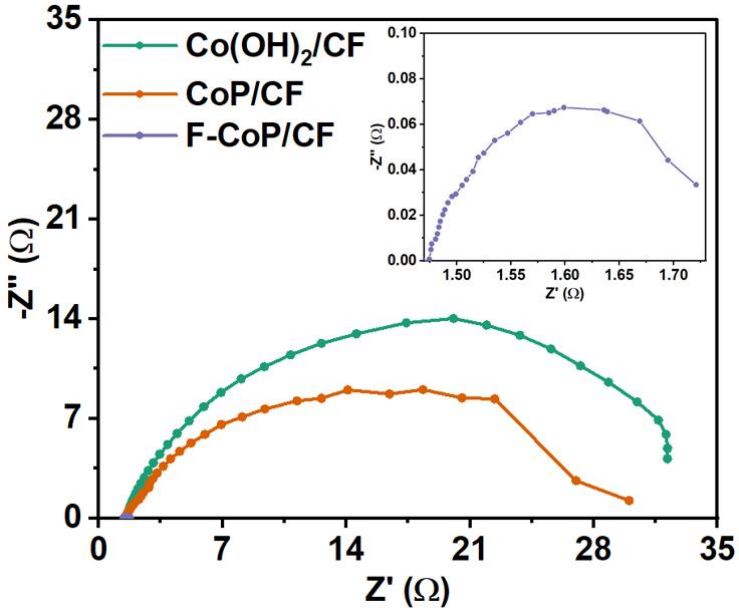

Figure S10 Nyquist plots of $Co(OH)_2$/CF, CoP/CF and F-CoP/CF.

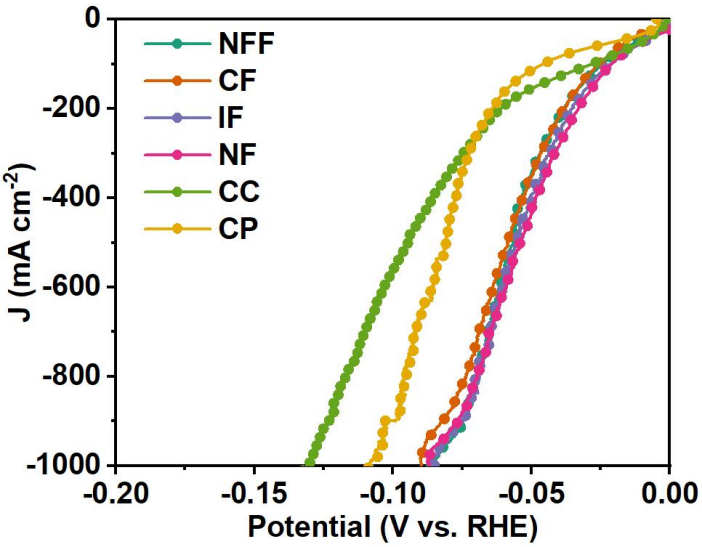

Figure S11 The HER performance for F-CoP samples on different substrates.

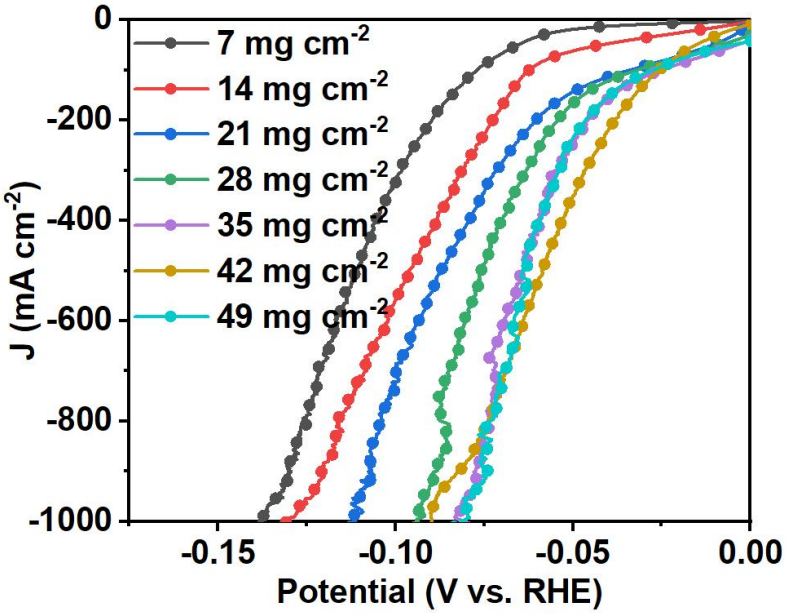

Figure S12 The HER performance of F-CoP/CF with different loading mass.

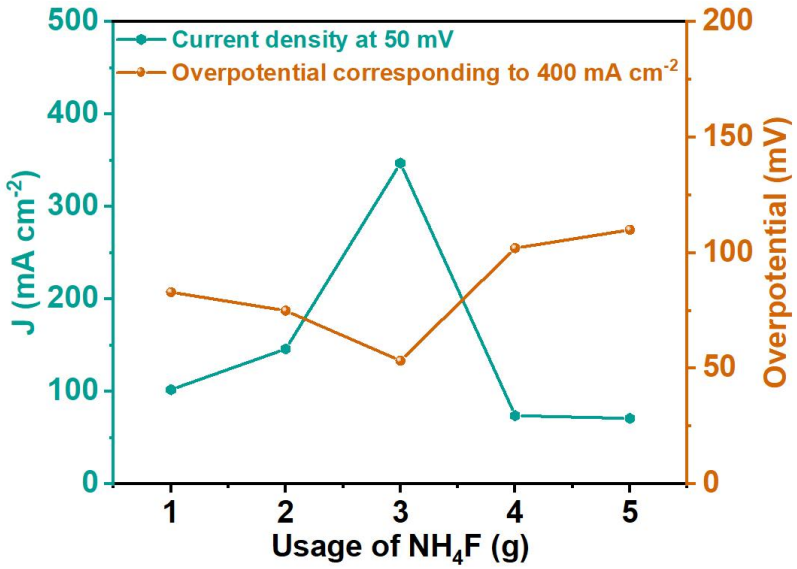

Figure S13 Comparison of HER performance of F-CoP/CF synthesized from different usages of NH_4F.

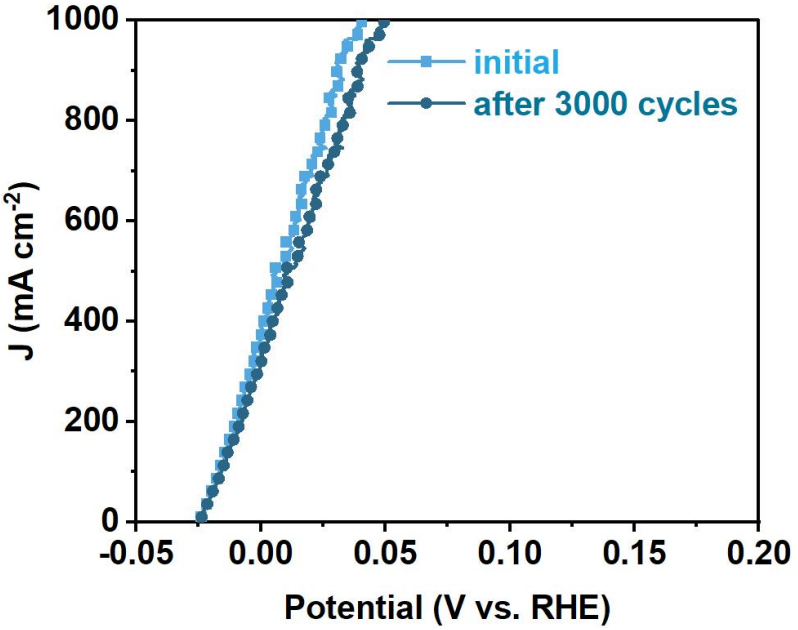

Figure S14 LSV curves of F-CoP/CF before and after 3000 cycles for HzOR.

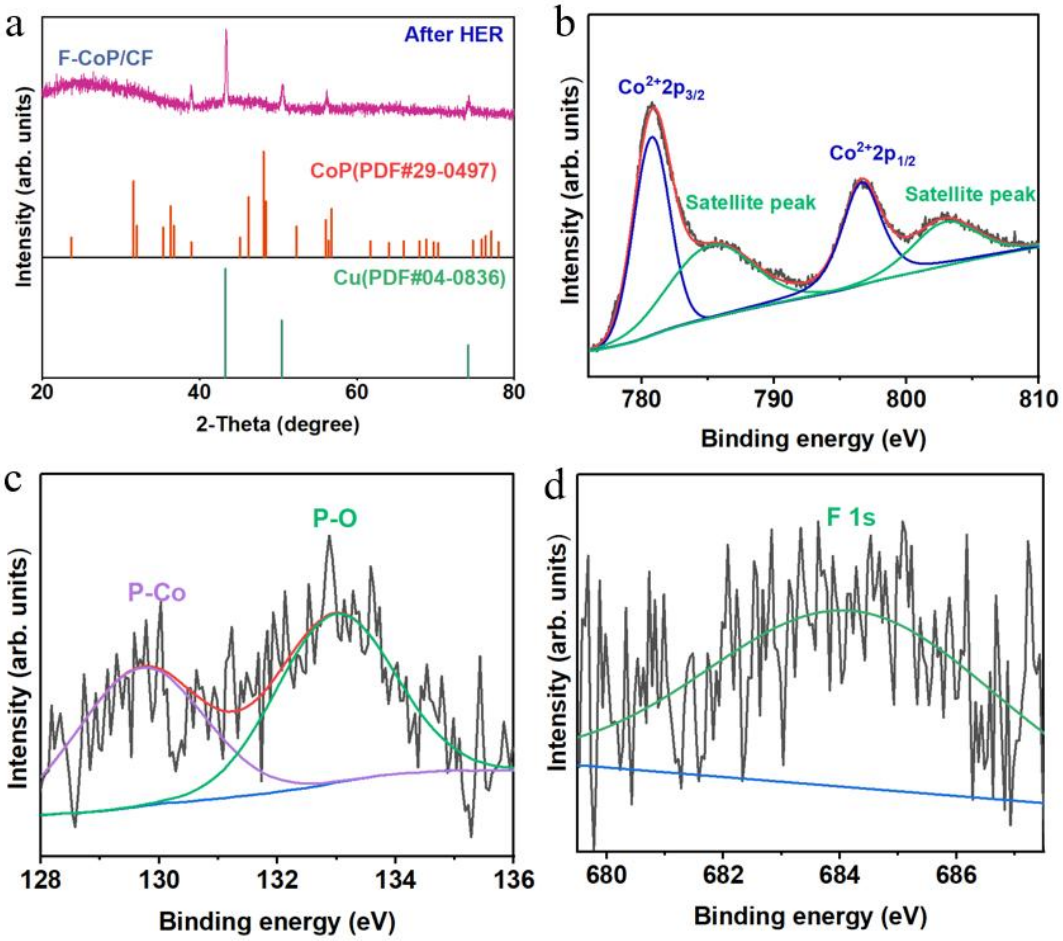

Figure S15 (a) The XRD pattern and (b-d) XPS spectra of F-CoP/CF sample after the stability test of HER.

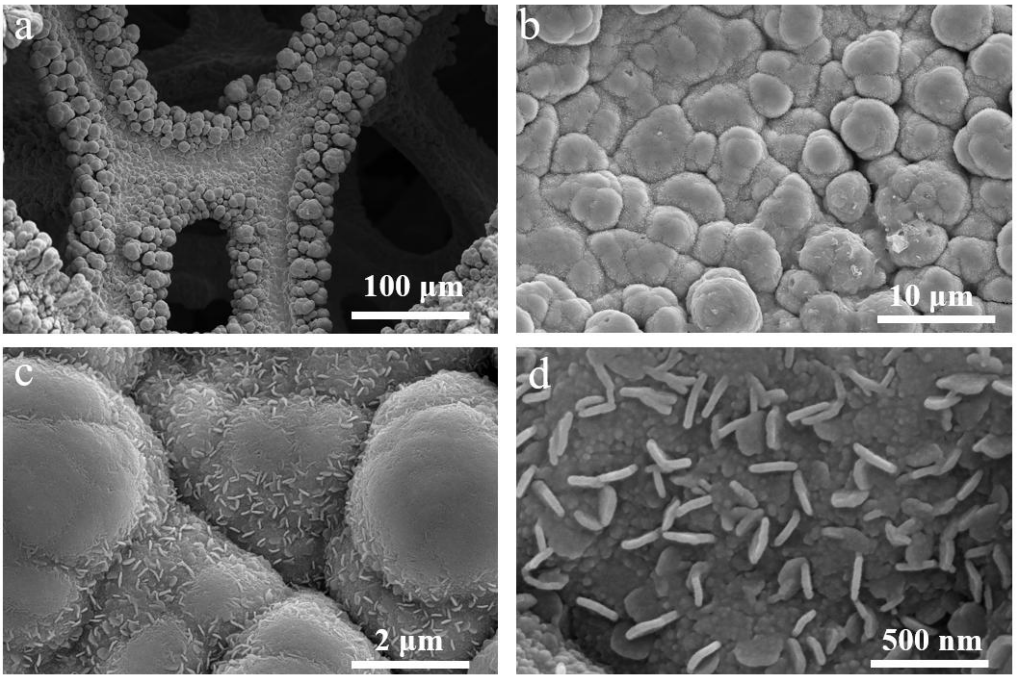

Figure S16 (a-d) The SEM images of F-CoP/CF sample after the stability test of HER.

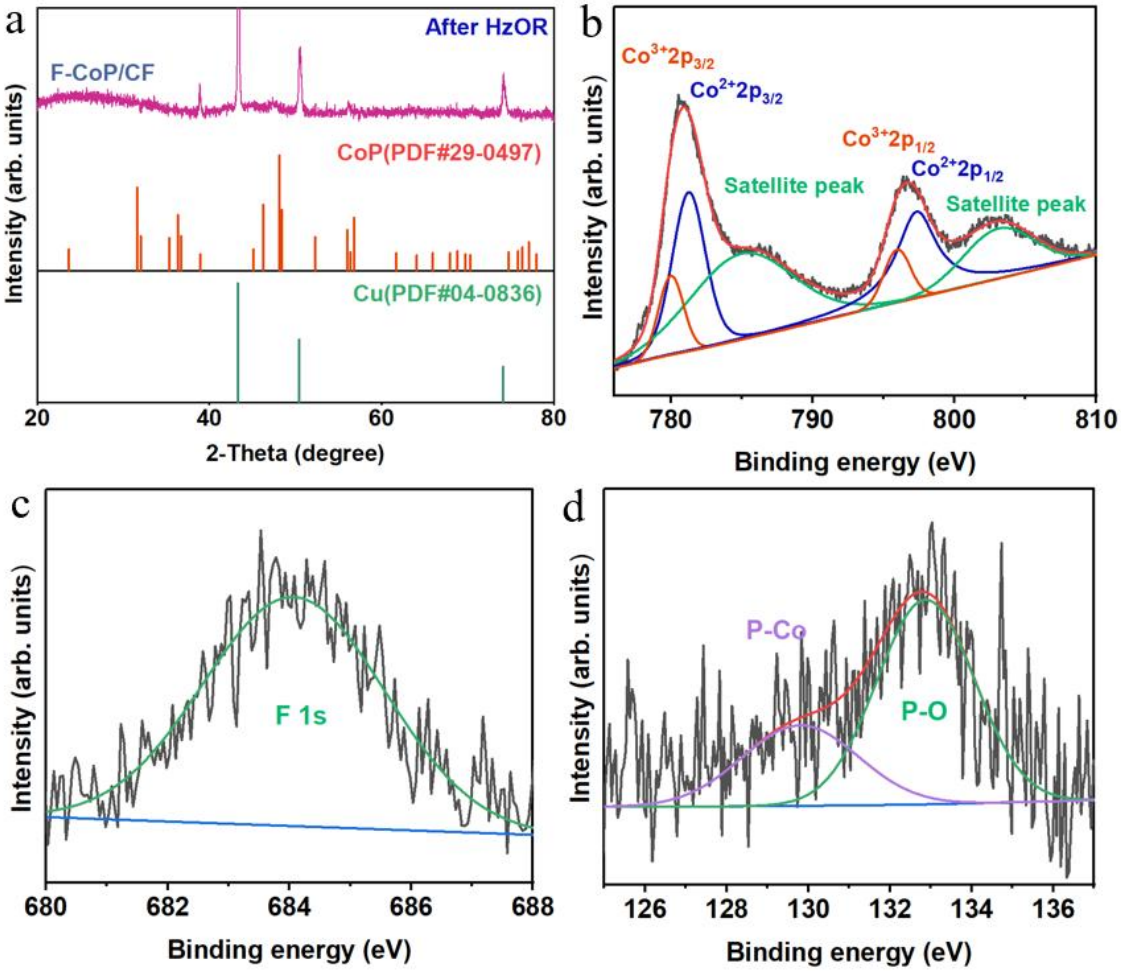

Figure S17 (a) The XRD pattern and (b-d) XPS spectra of F-CoP/CF sample after the stability test of HzOR.

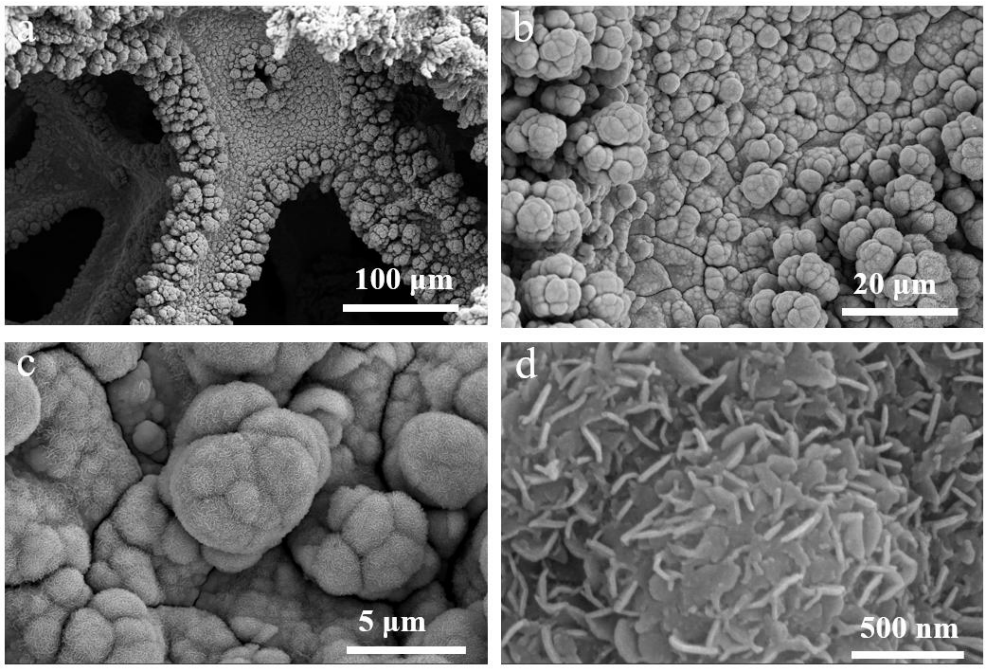

Figure S18 (a-d) The SEM images of F-CoP/CF sample after the stability test of HzOR.

Table S1 The fitting data of EIS spectra for the prepared catalysts for HER.

Catalysts	R_s (Ω)	R_0 (Ω)	R_1 (Ω)	CPE_1 (F)	CPE_2 (F)	R_{ct} (Ω)
F-CoP/CF	1.57	3.51E-5	2.00E-7	9.49E-5	4.70E-5	0.25
Cl-CoP/CF	1.50	4.00E-4	4.49E-5	1.27E-5	1.76E-4	0.49
Br-CoP/CF	1.59	1.41E-5	1.53E-4	9.36E-3	3.88E-5	1.01

Table S2 The fitting data of EIS spectra for the prepared catalysts for HzOR.

Catalysts	R_s (Ω)	R_0 (Ω)	R_1 (Ω)	CPE_1 (F)	CPE_2 (F)	R_{ct} (Ω)
CF	1.645	39.05	3.646	8.30E-4	5.03E-4	19.6
$Co(OH)_2$/CF	1.506	2.82E-6	5.431	5.55E-5	0.11	3.5
CoP/CF	1.513	2.99	1.47E-14	0.66	4.02E-5	2.1
F-CoP/CF	1.571	2.83E-5	8.25E-6	6.70E-5	8.64E-7	0.28

Table S3 Comparisons of HER performance of our catalysts with various kinds of reported earth abundant electrocatalysts.

Electrocatalyst	η_{10} (mV)	η_{200} (mV)	Tafel slope (mV dec^{-1})	Electrolyte	References
F-CoP/CF	5	38	28	1.0 M KOH	This work
Pt_3Ni	29	60	13	1.0 M KOH	[10]
NiCo-$MoNi_4$	75	300	67	1.0 M KOH	[11]
G@$MoNi_4$-$NiMoO_4$	55	250	38	1.0 M KOH	[12]
$MoNi_4$-600	80	200	45	1.0 M KOH	[13]
$MoNi_4$@MoO_{3-x}	80	350	45	1.0 M KOH	[14]
$MoNi_4$	10	50	30	1.0 M KOH	[15]
$MoNi_4$-MX_{10}	100	400	56	1.0 M KOH	[16]
Vs-Co_3S_4@NF	275	410	66	1.0 M KOH	[17]
P-NiMoS	225	285	91	1.0 M KOH	[18]
Co,Nb-MoS_2/TiO_2 HSs	200	240	40	1.0 M KOH	[19]
CuAlNiMoFe	56	90	60	1.0 M KOH	[20]
CoP/NiCoP/NC	200	560	64	1.0 M KOH	[21]
CPN@TC	55	265	30	1.0 M KOH	[22]
Ru/Ni/WC@NPC	93	297	33	1.0 M KOH	[23]
Co-Fe_2P	150	375	59	1.0 M KOH	[24]

Table S4 Performance comparisons of water splitting of our catalysts with other reported bifunctional electrodes.

Electrodes	Cell voltage (V) at 50 mA cm^{-2}	Cell voltage (V) at 200 mA cm^{-2}	electrolyzer	References
F-CoP/CF	0.05	0.14	H Cell	This work
F-CoP/CF	0.024	0.11	MEA	This work
PW-Co_3N NWA/NF	0.11	0.31	H Cell	[25]
Cu_1Ni_2-N	0.85	1.2	H Cell	[26]
Fe-$CoSe_2$	0.43	0.75	H Cell	[27]
$CoSe_2$	0.1	0.3	H Cell	[28]
Ni(Cu)	0.28	0.6	H Cell	[29]
Ni_2P	0.4	0.6	H Cell	[30]
CoSe/CP	0.5	0.75	H Cell	[31]
NiCo-$MoNi_4$	0.2	0.45	H Cell	[32]
$FeWO_4$-WO_3/NF	0.2	0.42	H Cell	[33]
Ru-FeP_4/IF	0.2	0.35	H Cell	[34]
Ni_2P-HNTs/NF	0.15	0.35	H Cell	[35]
NiS_2/TiM	0.55	0.95	H Cell	[36]
Mo-Ni_3N/Ni/NF	0.2	0.35	H Cell	[37]
Ni(Cu)@NiFeP/NM	0.35	0.75	H Cell	[38]
Ni_3N-Co_3N/NF	0.25	0.5	H Cell	[39]

References

[1] Kresse, G. and Joubert, D. From ultrasoft pseudopotentials to the projector augmented-wave method. *Phys. Rev. B* **59**, 1758-1775 (1999).

[2] Kresse, G. and Hafner, J. Ab initio molecular dynamics for liquid metals. *Phys. Rev. B* **47**, 558-561 (1993).

[3] Kresse, G. and Furthmuller, J. Efficient iterative schemes for ab initio totalenergy calculations using a plane-wave basis set. *Phys. Rev. B* **54**, 11169-11186(1996).

[4] Perdew, J. P. Density-Functional Approximation for the Correlation-Energy of the Inhomogeneous Electron-Gas. *Phys. Rev. B* **33**, 8822-8824 (1986).

[5] Perdew, J. P. and Burke, K. and Ernzerhof, M. Generalized Gradient Approximation Made Simple. *Phys. Rev. Lett.* **77**, 3865-3868 (1996).

[6] Monkhorst, H. J. and Pack, J. D. Special points for brillouin-zone integrations. *Phys. Rev. B* **13**, 5188-5192 (1976).

[7] Nørskov, J. K. et al. Origin of the overpotential for oxygen reduction at a fuelcell cathode. *J. Phys. Chem. B* **108**, 17886-17892 (2004).

[8] Wang, Z. et al. Single Ru atoms with precise coordination on a monolayer layered double hydroxide for efficient electrooxidation catalysis. *Chem. Sci.* **10**, 378-384 (2019).

[9] Johnson III, R. D. Computational chemistry comparison and benchmark database. http://cccbdb.nist.gov/. (2019).

[10] Li X, Huang Y, Chen Z, et al. Novel PtNi nanoflowers regulated by a third element (Rh, Ru, Pd) as efficient multifunctional electrocatalysts for ORR, MOR and HER[J]. *Chin. J. Chem. Eng*, **2023**, 454: 140131.

[11] Qian Q, Li Y, Liu Y, et al. Hierarchical multi-component nanosheet array electrode with abundant NiCo/$MoNi_4$ heterostructure interfaces enables superior bifunctionality towards hydrazine oxidation assisted energy-saving hydrogen generation[J]. *Chin. J. Chem. Eng*, **2021**, 414: 128818.

[12] An L, Zang X, Ma L, et al. Graphene layer encapsulated $MoNi_4$-$NiMoO_4$ for electrocatalytic water splitting[J]. *Appl. Surf. Sci*, **2020**, 504: 144390.

[13] Jin Y, Yue X, Shu C, et al. Three-dimensional porous $MoNi_4$ networks constructed by nanosheets as bifunctional electrocatalysts for overall water splitting[J]. *J. Mater. Chem. A*, **2017**, 5(6): 2508-2513.

[14] Wei J, Jia Q, Chen B, et al. High-efficient electrocatalyst of $MoNi_4$@ MoO_{3-x} nanorod for hydrogen evolution reaction in alkaline solutions[J]. *J. Alloys Compd*, **2021**, 876: 160152.

[15] Zhang J, Wang T, Liu P, et al. Efficient hydrogen production on $MoNi_4$ electrocatalysts with fast water dissociation kinetics[J]. *Nat.Commun*, **2017**, 8(1): 15437.

[16] Zhao X, Tang K, Lee C, et al. Promoting the Water‐Reduction Kinetics and Alkali Tolerance of $MoNi_4$ Nanocrystals via a $Mo_2TiC_2T_x$ Induced Built‐In Electric Field[J]. *Small*, **2022**, 18(15): 2107541.

[17] Wang G, Chen J, Cai P, et al. A self-supported Ni–Co perselenide nanorod array as a high-activity bifunctional electrode for a hydrogen-producing hydrazine fuel cell[J]. *J. Mater. Chem. C*, **2018**, 6(36): 17763-17770.

[18] Wang Z, Xu L, Huang F, et al. Copper–nickel nitride nanosheets as efficient bifunctional catalysts for hydrazine‐assisted electrolytic hydrogen production[J]. *Adv. Energy Mater*, **2019**, 9(21): 1900390.

[19] Shen F, Wang Z, Wang Y, et al. Highly active bifunctional catalyst: Constructing $FeWO_4$-WO_3 heterostructure for water and hydrazine oxidation at large current density[J]. *Nano Research*, **2021**, 14(11): 4356-4361.

[20] Cui T, Chi J, Zhu J, et al. Tuning the size and chemisorption of FeP_4 by trace Ru doping for hydrazine-assisted hydrogen evolution in seawater at large‐current‐density[J]. *Appl. Catal. B*, **2022**, 319: 121950.

[21] Wang T J, Xu G R, Sun H Y, et al. Anodic hydrazine electrooxidation boosted overall water electrolysis by bifunctional porous nickel phosphide nanotubes on nickel foam[J]. *Nanoscale*, **2020**, 12(21): 11526-11535.

[22] Wang J, Ma X, Liu T, et al. NiS_2 nanosheet array: A high-active bifunctional electrocatalyst for hydrazine oxidation and water reduction toward energy-efficient hydrogen production[J]. *Mater. Today Phys*, **2017**, 3: 9-14.

[23] Liu Y, Zhang J, Li Y, et al. Realizing the Synergy of Interface Engineering and Chemical Substitution for Ni_3N Enables its Bifunctionality Toward Hydrazine Oxidation Assisted Energy-Saving Hydrogen Production[J]. *Adv funct mater*, **2021**, 31(35): 2103673.

[24] Zhang H, Wang J, Qin F, et al. V-doped Ni_3N/Ni heterostructure with engineered interfaces as a bifunctional hydrogen electrocatalyst in alkaline solution: Simultaneously improving water

dissociation and hydrogen adsorption[J]. *Nano Res.*, **2021**, 14(10): 3489-3496.

[25] Qian Q, Zhang J, Li J, et al. Artificial heterointerfaces achieve delicate reaction kinetics towards hydrogen evolution and hydrazine oxidation catalysis[J]. *Angew. Che*, **2021**, 133(11): 6049-6058.

[26] Wang Z, Xu L, Huang F, et al. Copper‐nickel nitride nanosheets as efficient bifunctional catalysts for hydrazine‐assisted electrolytic hydrogen production[J]. *Adv. Energy Mater*, **2019**, 9(21): 1900390.

[27] Liu X, He J, Zhao S, et al. Self-powered H_2 production with bifunctional hydrazine as sole consumable[J]. *Nat. Commun*, **2018**, 9(1): 1-10.

[28] Xia B, Zhang J, Wang H, et al. Substituted anodic hydrazine oxidation assisting energy-efficient hydrogen production based on bifunctional cobalt perselenide nanosheet electrode[J]. *Angew. Chem*, **2018**, 130: 7775-7779.

[29] Sun Q, Wang L, Shen Y, et al. Bifunctional copper-doped nickel catalysts enable energy-efficient hydrogen production via hydrazine oxidation and hydrogen evolution reduction[J]. *Acs sustain chem eng*, **2018**, 6(10): 12746-12754.

[30] Tang C, Zhang R, Lu W, et al. Energy‐saving electrolytic hydrogen generation: Ni_2P nanoarray as a high‐performance non‐noble‐metal Electrocatalyst[J]. *Angew. Chem. Int. Ed*, **2017**, 56(3): 842-846.

[31] Pu Z, Amiinu I S, Gao F, et al. Efficient strategy for significantly decreasing overpotentials of hydrogen generation via oxidizing small molecules at flexible bifunctional CoSe electrodes[J]. *Journal of Power Sources*, **2018**, 401: 238-244.

[32] Wang G, Chen J, Cai P, et al. A self-supported Ni–Co perselenide nanorod array as a high-activity bifunctional electrode for a hydrogen-producing hydrazine fuel cell[J]. *J. Mater. Chem. C*, **2018**, 6(36): 17763-17770.

[33] Shen F, Wang Z, Wang Y, et al. Highly active bifunctional catalyst: Constructing $FeWO_4$-WO_3 heterostructure for water and hydrazine oxidation at large current density[J]. *Nano Research*, **2021**, 14(11): 4356-4361.

[34] Cui T, Chi J, Zhu J, et al. Tuning the size and chemisorption of FeP_4 by trace Ru doping for hydrazine-assisted hydrogen evolution in seawater at large‐current‐density[J]. *Appl. Catal. B*, **2022**, 319: 121950.

[35] Wang T J, Xu G R, Sun H Y, et al. Anodic hydrazine electrooxidation boosted overall water

electrolysis by bifunctional porous nickel phosphide nanotubes on nickel foam[J]. *Nanoscale*, **2020**, 12(21): 11526-11535.

[36] Wang J, Ma X, Liu T, et al. NiS_2 nanosheet array: A high-active bifunctional electrocatalyst for hydrazine oxidation and water reduction toward energy-efficient hydrogen production[J]. *Mater. Today Phys*, **2017**, 3: 9-14.

[37] Liu Y, Zhang J, Li Y, et al. Realizing the Synergy of Interface Engineering and Chemical Substitution for Ni_3N Enables its Bifunctionality Toward Hydrazine Oxidation Assisted Energy-Saving Hydrogen Production[J]. *Adv funct mater*, **2021**, 31(35): 2103673.

[38] Zhang H, Wang J, Qin F, et al. V-doped Ni_3N/Ni heterostructure with engineered interfaces as a bifunctional hydrogen electrocatalyst in alkaline solution: Simultaneously improving water dissociation and hydrogen adsorption[J]. *Nano Res.*, **2021**, 14(10): 3489-3496.

[39] Qian Q, Zhang J, Li J, et al. Artificial heterointerfaces achieve delicate reaction kinetics towards hydrogen evolution and hydrazine oxidation catalysis[J]. *Angew. Chem. Int. Ed*, **2021**, 133(11): 6049-6058.